

MFIF-GAN: A New Generative Adversarial Network for Multi-Focus Image Fusion

Yicheng Wang, Shuang Xu, Junmin Liu*, Zixiang Zhao, Chunxia Zhang,
Jiangshe Zhang

School of Mathematics and Statistics, Xi'an Jiaotong University

Abstract

Multi-Focus Image Fusion (MFIF) is one of the promising techniques to obtain all-in-focus images to meet people's visual needs and it is a precondition of other computer vision tasks. One of the research trends of MFIF is to solve the defocus spread effect (DSE) around the focus/defocus boundary (FDB). In this paper, we present a novel generative adversarial network termed MFIF-GAN to translate multi-focus images into focus maps and to get the all-in-focus images further. The *Squeeze* and *Excitation* Residual Network (SE-ResNet) module as an attention mechanism is employed in the network. During the training, we propose reconstruction and gradient regularization loss functions to guarantee the accuracy of generated focus maps. In addition, by combining the prior knowledge of training condition, this network is trained on a synthetic dataset with DSE based on an α -matte model. A series of experimental results demonstrate that the MFIF-GAN is superior to several representative state-of-the-art (SOTA) algorithms in visual perception, quantitative analysis as well as efficiency.

Keywords: multi-focus image fusion, defocus spread effect, generative adversarial network, deep learning.

*Corresponding author

Email address: junminliu@mail.xjtu.edu.cn (Junmin Liu)

1. Introduction

In the field of digital photography, depth-of-field (DOF) is the distance between the nearest and the farthest objects that are in acceptably sharp focus [1]. However, the limited DOF leads to multi-focus regions and the defocus spread effect (DSE) [2]. An example of the couple source images (a) (b) and the desired result (c) are shown in Fig.1.

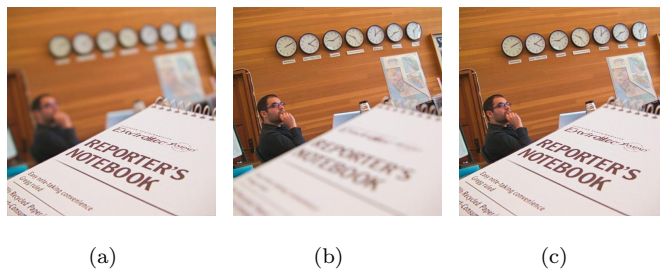


Figure 1: The source of MFIF images and desired fusion result

To address this problem, MFIF has been studied as a technique to fuse multiple images focused at different regions or depths in the same scene, so that the obtained fused all-in-focus images retain the clear information of the source images. It is a pre-condition for various kinds of computer vision tasks, such as localization, object detection, recognition and segmentation[3, 4].

The past few decades have witnessed the rapid development of abundant MFIF algorithms. Generally, the classic MFIF algorithms can be categorized into two groups: transform domain and spatial domain methods [5]. The idea of the former is to transform the images from original image space into an abstract feature space so that the active level of source images can be detected and measured easily. Then a desired image is reconstructed from feature space into image space after merging the active feature according to a certain fusion strategy [2]. The typical transform domain MFIF methods include the non-subsampled contourlet transform (NSCT) methods [6, 7], the sparse representation (SR) methods [8, 9] and the combined NSCT-SR method [10]. The drawback is that these algorithms often produce non-realistic results, even in

the areas far away from the FDB [11].

Apart from the first group, the spatial domain methods mainly include pixel-based, block-based and region-based algorithms [12]. Because in the field of MFIF, it is assumed that each pixel, block or region is either focused or defocused [13]. Hence, they aim at determining the FDB precisely.

The pixel-based image fusion methods generally employ a focus measure to detect the focused pixels from the source images and generate the decision maps or weight maps¹. Then some refinement algorithms, such as guided filtering [14], are utilized as post-processing to correct the decision maps. Finally, the all-in-focus images are fused by refined decision maps acting on the source images. The pixel-based methods are usually sensitive to noise because of ignoring the information about the spatial neighbors.

The block-based image fusion algorithms crop the source images into same blocks. Then the focused blocks are determined by comparing the focus measure of the corresponding blocks. However, block-based techniques generally are sensitive and restricted to the block-size [12]. In order to avoid the problem of the block-size selection, De et al. [12] and Bai et al. [15] proposed adaptive block-based algorithms through a quad-tree structure to further divide the blocks between focused and defocused to find out the focus maps.

The region-based algorithms, such as boundary finding based methods [16], firstly segment the source images by image segmentation techniques, and then image fusion is performed by measuring clarity of the corresponding regions and combining the detected focused regions. However, the efficiency and performance of the region-based algorithms are usually influenced by the segmentation procedures.

In the past few years, Deep Learning (DL) has aroused researchers widespread interests for its surprising effectiveness in computer vision (CV) applications. Liu et al. [17] made the first attempt to use convolutional neural networks (CNNs) for MFIF. In their work, the siamese architecture was used to extract

¹They are essentially same as the focus map mentioned in the rest of this paper.

the feature of the focused and defocused regions. Guo et al. [18] proposed a fully convolutional network for focus detection. Inspired by the DL tools and region based methods, deep semantic segmentation and edge detection algorithms [19, 20] are employed in MFIF to capture the clear focus maps.

At present, one of the important research trends of MFIF is to solve the DSE around the FDB and to get higher quality fusion images further. Actually, the DSE describes a common phenomenon that regions far away from the FDB are focused or defocused totally, while in patches near the FDB, focused and defocused area may exist simultaneously [19]. In other words, this boundary sometimes is a ribbon region with uncertain width instead of a clear curve.

More precisely, when the foreground is in focus, the blurred background object will not influence the clear foreground object, that is, the boundary of FDB is clear as displayed in Fig.2(a) I_A . However, when the foreground is defocused, the blurred foreground will permeate the background. Obviously, blurred foreground object is mildly bigger than itself as shown in Fig.2(b) I_B .



Figure 2: I_A without DSE and I_B suffers from DSE

In this paper, we present a new MFIF algorithm termed MFIF-GAN which is fed with color source images and output the fused all-in-focus image. This algorithm adopt Squeeze and Excitation (SE) block based SE-ResNet [21] as attention mechanism. The reconstruction loss and gradient penalty are utilized to acquire images with higher quality. In the end, the generated initial focus maps are processed by small region removal as a post-processing algorithm in a computational efficient manner. In order to further improve the quality of the

fused images, we synthesize a large-scale training set suffering from the DSE by applying an α -matte boundary defocus model [11] to the VOC 2012 dataset [22].

Several experiments are carried out to verify the performance of our network. The results demonstrate that MFIF-GAN outperforms several typical SOTA algorithms regarding 12 evaluation metrics. And the images fused by MFIF-GAN are also better than other methods visually. In addition, a series of ablation experiments are conducted to study the role of each module in our network.

The contributions of this paper are as follows:

1. A new color image fusion algorithm used SE-blocks as attention mechanism is proposed. The loss function added with the ℓ_1 -norm reconstruction and gradient penalty is used innovatively.
2. A more realistic training dataset with DSE is constructed using an α -matte model which can be a new benchmark training dataset for other supervised algorithms.
3. Training on this new dataset makes a better performance around the FDB visually and on the corresponding metrics than several existing SOTA methods.
4. The computationally lightweight post-processing is directly incorporated into the fusion algorithm. The fusion speed of this algorithm is highest with respect to the above methods.

The rest of this paper is arranged as follows. In section 2, a briefly review of the related works is provided in which the α -matte model, FuseGAN and attention mechanisms are introduced. And the deficiencies of the baseline work FuseGAN are discussed. Section 3 describes the details of the proposed network. Then, experiments are conducted in section 4 to evaluate the proposed method both in qualitative and quantitative. And the necessary of some contents in the network is discussed in ablation experiments. At last discussions and conclusions are drawn in section 5.

2. Related Works

2.1. α -matte Model for MFIF Datasets

Due to the lack of the large scale datasets of multi-focus images, several data generation methods based on public natural image datasets were adopted in many CNN based algorithms [13, 17, 23, 24, 25] to meet the actual requirements. For example, in FuseGAN [13], a multi-focus image dataset was synthesized based on PASCAL VOC 2012 dataset [22]. Guo et al. and Fidel et al. used CIFAR-10 and MS COCO respectively to constructed MFIF training datasets [26, 18].

However, none of them take the DSE into account. The unrealistic training data may limit the performance of theses algorithms [11]. Recently, Ma et al. [11] proposed a novel α -matte model which provides a insightful perspective to understand DSE and real world multi-focus images. In addition, this model can easily generate couple images as training datasets with DSE. More details about training data generation is discussed in section 4.1.1.

2.2. FuseGAN for Multi-Focus Images to Focus Map Translation

Inspired by the conditional generative adversarial network (cGAN) [27] for image-to-image task, FuseGAN [13] was proposed to solve the MFIF task. Given the requirement of dual inputs and single output, the encoder of the generator in FuseGAN proposed is designed as a siamese network like [17]. Then the objective function of LSGAN [28] was employed. At last, a convolutional conditional random fields (ConvCRFs) based technique [29] was exploited to refine the initial focus maps. Compared with other spatial domains methods (BF [16], DSIFT [30], CNN [17]), the focus region detected by FuseGAN is closer to the ground truth. In our experiments, FuseGAN is regarded as a baseline network.

The disadvantages of FuseGAN are summarized as follows. (1) It is designed for gray images. Obviously, this will lose important color information and it may limit the application of the method. (2) The adversarial loss of FuseGAN is borrowed from LSGAN. It is worth noting that the distinction between images

will be excessively magnified by ℓ_2 -norm, which makes the training unstable. (3) As for the additional reconstruction loss, the coefficient λ_{rec} of the binary cross entropy loss in the loss function of generator is set very large which has no interpretability. And Aritra Ghosh et al. [31] argued that the cross entropy loss is commonly sensitive to label noise in classification tasks. (4) Last but not least, FuseGAN exploited ConvCRFs to refine initial focus maps. It should be noted that ConvCRFs will break down if the all-in-focus images as ground truth are not available. So it often leads to unsatisfactory results in the real applications.

2.3. Attention Mechanisms and SENet

Apart from traditional CNNs, some researches attend to strengthen the representation of networks to focus on salient objects in images for particular tasks. It should be precisely noted that in MFIF issues, the procedure of producing a retioinal focus map equates finding the objects which are in or out of focus.

As an attention mechanism, Hu et al. proposed the SE block [21] consisting of a *squeeze* and a *excitation* operation, which model the interdependencies between the channels of feature maps to recalibrate them. The first squeeze module outputs a global distribution of features by aggregating feature maps across spatial dimensions. And using a gating mechanism, the excitation operation produces a collection of weights which represents the relationships between the channels of features.

Meanwhile, with the flexible nature, the SE block could be directly integrated into other network architectures such as residual networks [32] and inception networks [33] as atomic building blocks. And experiments have demonstrated that the basic SE-ResNet module could bring significant improvement with respect to existing CNNs in a computational efficient way. In our work, this module is exploited in the parallel network structure to extract the implicit features with multi-channels.

3. The Proposed Method

Lots of previous MFIF algorithms have achieved good fusion performances, but few works take the DSE into account. For example, an unsupervised generative adversarial network [34] as a similar work compared with ours which has complex structure and well-designed loss function do not analyse the essence of the DSE. In this section, we propose a novel GAN-based network for the MFIF task, especially for alleviating the DSE. To begin with, we introduce the symbols used in this paper.

Let I stand for the all-in-focus image. In the synthetic training set, it is regarded as the ground truth. The binary matrix F represents a focus map, where $F_{ij} = 1$ if (i, j) pixel is in focus and 0 otherwise. The focus map generated by the network and the one refined by post-processing are denoted by \hat{F} and \hat{F}_{final} respectively. One of the source images I_A corresponds to the one which has a clear foreground with a blurred background. While another source image I_B suffering from the DSE has a blurred foreground with a clear background.

3.1. Architecture of the Network

As a variant of GAN [35], MFIF-GAN also consists of two fundamental modules: a generator and a discriminator. The architecture of proposed MFIF-GAN is shown in Fig.3. The generator in MFIF-GAN is fed with the source color images I_A and I_B aiming to generate focus map \hat{F} . The input of the discriminator is the concatenation of I_A , I_B and the (ground truth or generated) focus map. In our work, the aim of the generator is to reconstruct focus maps as accurately as possible, while the purpose of the discriminator is to distinguish the generated focus maps from the real ones.

Generator G : The G includes an encoder, a tensor concatenation module and a decoder. In order to effectively process color images, the encoder is designed as six branches of parallel sub-networks sharing parameters for each channel of source images.

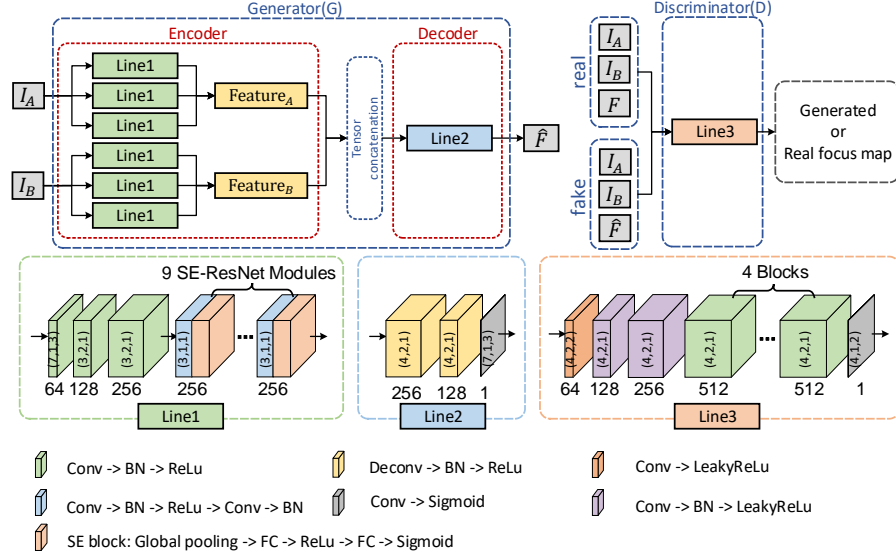


Figure 3: The work flow of the training and the detail architecture of MFIF-GAN. The convolution layer, transposed convolution layer, BatchNorm layer, Rectified Linear Unit and fully connected layer are denoted as Conv, Deconv, BN, ReLU and FC respectively. The number under every block represents the channel number of Conv or Deconv. The array in bracket on every block indicates the kernel, stride and padding size of Conv or Deconv respectively.

Each sub-network in encoder is composed of three convolutional modules and nine residual blocks. In order to reduce computation burden, the 2nd and 3rd convolutional modules with a stride of 2 down-sample feature maps. Furthermore, inspired by SE-Net [21] as an attention mechanism, each residual block is equipped with a SE block as SE-ResNet module to find the interdependencies between the channels of feature maps and extract the most informative components of the images. In every SE-ResNet module, the SE block is attached to the non-identity branch which is a defaulted residual module with two convolutional layers and batch normalization (BatchNorm) [36] to guarantee the squeeze and excitation module work before addition with the identity branch.

In the tensor concatenation part, six feature maps extracted by the en-

coder from each channel are averaged to obtain the global features $Feature_A$, $Feature_B$ of I_A and I_B , respectively. Then, this two features are concatenated on third channel.

In the decoder layer, the concatenated features are upsampled and deconvolved through two transposed convolutional layers for reconstruction. Finally, the single-channel focus map is outputted by a convolutional and activating layer.

Discriminator D : In the discriminator, eight convolutional layers are used to compress the input data continuously until the final sigmoid activation function is used to judge the input focus map is real or generated. Specifically, the input is a 7-channel tensor, i.e., the concatenation of source images and a focus map generated by G or the real one from the training dataset. The padding and stride size of convolutional layers for down-sampling is set to guarantee the final output is a single element for judgment.

3.2. Loss Function

The objective function plays an important role in deep learning. Some works indicated the original GAN suffers from training instability because of the loss function. That is, during the D and G is trained to optimality alternately, the Jensen-Shannon divergence between the real data distribution \mathbb{P}_{data} and the noise distribution \mathbb{P}_z is minimized [35], which often leads to vanishing gradients. As a improved GAN, WGAN [37] still suffers from either vanishing or exploding gradients without retional tuning of the clipping threshold c [38].

So in our work, we adopted the improved training of WGAN [38], the adversarial loss function of D and G are listed as equation 1 and 2 respectively:

$$\mathcal{L}_{adv}(D) = \mathbb{E}_{I,F \sim \mathbb{P}_{I,F}}[D(I, F)] - \mathbb{E}_{I \sim \mathbb{P}_I}[D(I, G(I))] \quad (1)$$

$$\mathcal{L}_{adv}(G) = -\mathbb{E}_{I \sim \mathbb{P}_I}[D(I, G(I))] \quad (2)$$

where $I, F \sim \mathbb{P}_{I,F}$ in 1 denotes the inputs of D follow the joint distribution of the images and focus maps from the real data.

As the main contribution in their work, the gradient penalty \mathcal{L}_{gp} is added into the loss function of D to stabilize the training process and further improve the quality of generated focus maps. That is:

$$\mathcal{L}_{gp} = \mathbb{E}_{I, \tilde{F} \sim \mathbb{P}_{I, \tilde{F}}} [(\|\nabla_{\tilde{F}} D(I, \tilde{F})\|_2 - 1)^2] \quad (3)$$

where \tilde{F} is sampled uniformly along a straight line between a pair of the focus map F and the generated one \hat{F} .

According to [31], compared with cross entropy loss used in FuseGAN, the loss function based on mean absolute value of error is more robust to noise. Therefore, as for G , we employ the ℓ_1 -norm as reconstruction loss \mathcal{L}_{rec} to measure the difference between the generated focus maps and the real ones, as shown in equation 4:

$$\mathcal{L}_{rec} = \mathbb{E}_{I, F \sim \mathbb{P}_{I, F}} [|F - G(I)|] \quad (4)$$

So the total loss functions of MFIF-GAN can be defined by equations 5 and 6:

$$\min_D \mathcal{L}(D) = \mathcal{L}_{adv}(D) + \lambda_{gp} \mathcal{L}_{gp} \quad (5)$$

$$\min_G \mathcal{L}(G) = \mathcal{L}_{adv}(G) + \lambda_{rec} \mathcal{L}_{rec} \quad (6)$$

We use $\lambda_{gp} = 10$ defaulted in [38] for all experiments. In order that λ_{gp} and λ_{rec} are used to adjust these two additional loss terms to the same level of importance, the value of λ_{rec} is set as same as λ_{gp} .

3.3. Post-processing in MFIF-GAN

The initial focus maps generated by G often suffer from mis-registration or noise resulting in an unsatisfactory fusion image. Hence, the initial focus maps need refinement. We employ the small region removal (SRR) strategy. The SRR works on the binary matrix and it removes the region whose number of pixels is smaller than a threshold N . In this paper, we set $N = 0.001WH$, where W and H are the width and height of an image, respectively. After post-processing, the final focus maps \hat{F}_{final} can be obtained. This porcessing is so simple and effective that it does not increase computational burden.

4. Experiments

We conduct a series of experiments to verify the performance of the MFIF-GAN. The illustrations and tables will be discussed in detail to achieve the visual and quantitative comparison. In addition, the effectiveness and rationality of the proposed method have also been proved by ablation experiments.

4.1. Experiments Preparation

4.1.1. Dataset

Training a supervised neural network needs a large amount of samples with ground truth. However, to the best of knowledge, there still lacks publicly available MFIF training datasets which take the DSE into account. Therefore, we apply α -matte model [11] to the PASCAL VOC 2012 database [22] to construct a synthetic training dataset with DSE which will be termed α -matte dataset.

The PASCAL VOC 2012 is a well-known image segmentation database, each image of which corresponds to a segmentation map. We regard the binary segmentation map as a focus map F (matte α^C in [11]). Using the focus map F , the clear foreground FG^C and background BG^C can be get as follows:

$$FG^C = F * I \quad (7)$$

$$BG^C = (1 - F) * I \quad (8)$$

where $*$ means production pixel by pixel.

The blurred focus map F^B (matte α^B in [11]) can be obtained by applying a gaussian filter $G(x, y; \sigma)$ as kernel function to corresponding F . That is:

$$F^B = G(x, y; \sigma) \otimes F \quad (9)$$

where \otimes presents the convolution operator. The blurred foreground FG^B and background BG^B can be acquired in the same way.

Finally, according to the α -matte model, a pair of training images I_A and I_B with only two valid surface (foreground surface S_{FG} and background surface

S_{BG}) can be obtained by equations 10 and 11 respectively.

$$\begin{aligned}
I_A &= S_{FG}^{clear} + S_{BG}^{blurry} \\
&= FG^C + (1 - \alpha^C) * BG^B \\
&= F * I + (1 - F) * \{G(x, y; \sigma) \otimes [(1 - F) * I]\}
\end{aligned} \tag{10}$$

$$\begin{aligned}
I_B &= S_{FG}^{blurry} + S_{BG}^{clear} \\
&= FG^B + (1 - \alpha^B) * BG^C \\
&= G(x, y; \sigma) \otimes (F * I) + (1 - G(x, y; \sigma) \otimes F) * [(1 - F) * I]
\end{aligned} \tag{11}$$

In order to verify the influence of the training sets constructed by the α -matte model, basing on the general MFIF training dataset generation raised in [26], we synthesize an another dataset without DSE for the ablation experiment. In what follows, we call it conventional MFIF training dataset. In formula, the source images are obtained by 12 13.

$$I_A = F * I + (1 - F) * (G(x, y; \sigma) \otimes I) \tag{12}$$

$$I_B = F * (G(x, y; \sigma) \otimes I) + (1 - F) * I \tag{13}$$

As for testing data, the famous Lytro [39] dataset is utilized widely for its relatively high quality (basically meeting the requirements of multi-focus image with mild DSE). In addition, a new dataset called MFF in the wild (MFFW) [2] which significantly suffers from DSE is conducted in the test. In order to verify the performance of our algorithms comprehensively, 10 pairs of gray images termed grayscale in a survey of SOTA [40] is also used.

4.1.2. Training and Testing Paradigm

In the training stage, we optimize G and D alternately. In order to better optimize the objective function and simplify the updating strategy of learning rate, we use the adam with two parameters β_1 and β_2 which are initialized to 0.5 and 0.999, respectively. And the linear declining strategy is used to update the learning rates of G and D both initialized to 0.0001. Besides, the update rate ratio between G and D is 1 : 5, which means that G is updated once after updating D for five times.

In the testing phase, we only retain G followed by a post-processing SRR to generate the focus map \hat{F} and refine it. The processed focus map \hat{F}_{final} is used to extract the clear regions of the source images and reconstruct the all-in-focus images as followed:

$$I_{fused} = I_A * \hat{F}_{final} + I_B * (1 - \hat{F}_{final}) \quad (14)$$

For the grayscale dataset, samples are tripled to form images with 3 channels as inputs of G .

4.1.3. Experimental Process

Our network is compared with eight representative SOTA methods, including spetial domain methods Quadtree [15] and DSIFT [30], transform domain methods NSCT [6], CSR [41] and MWGF [42], deep learning based methods MMF-Net [11], FuseGAN [13] and CNN [17].

Specifically, MMF-Net only provides the fused images on Lytro dataset which can be directly use². Apart from DSIFT³, four methods(NSCT⁴, Quadtree⁵, CSR⁶ and MWGF⁷) are all designed for gray images. Therefore, we separately apply these algorithms to R, G and B channels of color images, and at last combine the fusion results on the third channels. As for CNN, we utilize the official codes and pre-trained weights⁸ to output the fused images.

At last, the official codes of FuseGAN are unavailable, so we re-implement and re-train FuseGAN by ourselves. Note that FuseGAN is trained on the conventional MFIF training dataset and the other fundamental training configuration is set as default.

²<https://github.com/xytmhy/MMF-Net-Multi-Focus-Image-Fusion>

³<http://www.escience.cn/people/liuyu1/Codes.html>

⁴<https://github.com/yuliu316316/MST-SR-Fusion-Toolbox>

⁵<https://github.com/uzeful/Quadtree-Based-Multi-focus-Image-Fusion>

⁶<http://www.escience.cn/people/liuyu1/Codes.html>

⁷https://www.researchgate.net/publication/307415978_MATLAB_Code_of_Our_Multi-focus_Image_Fusion_Algorithm_MWGF

Multi-focus_Image_Fusion_Algorithm_MWGF

⁸<http://home.ustc.edu.cn/~liuyu1>

4.2. Comparison with SOTA Methods

In this subsection, twelve objective evaluation metrics used to assess fusion images quality are briefly introduced and the detailed quantitative results with respect to the proposed MFIF-GAN and SOTA methods are then listed. To evaluate the performance of our network in visual perspective intuitively, the fusion results with detailed magnified of all methods are compared to verify the improvement of the proposed algorithm with regard to the DSE.

4.2.1. Quantitative Assessment Metrics

In order to assess the fusion performance of different algorithms comprehensively, twelve quantified metrics are used⁹. Which is mutual information MI [43], Tsallis entropy based metric TE [44], nonlinear correlation information entropy $NCIE$ [45], gradient-based metric Q_G [46], Q_M proposed by Pen-Wei Wang et al. [47], spatial frequency SF [48], structure similarity based metric $SSBM$ proposedal by Cui Yang et al. (also named Yang’s metric Q_Y) [49], Chen-blum metric Q_{CB} [50], linear index of fuzziness LIF [51], average gradient AG [52], mean square deviation MSD [24] and gray level difference GLD [24]. Detailed mathematical expressions for these metrics are not listed here due to the page limitation.

It is worth to note that the fused images assessed are better if all metrics are larger except for LIF . These metrics have different emphases, so none of them is better than all others. The first eight traditional metrics (i.e. MI , TE , $NCIE$, Q_G , Q_M , SF , Q_Y and Q_{CB}) are widely used in assessment of images quality for their characteristics of computing agreements of fused images with the sources.

In spite of the generalized employment of these metrics, some research demonstrated that they often lead to confused judgment [53]. Ignoring the existence of DSE, images fused by previous works cannot capture abundant in-

⁹The implementation of these metrics are available at <https://github.com/zhengliu6699/imageFusionMetrics>

formation existing around the FDB. And the measure of these narrow area is so small that conventional metrics which focus on overall image consistency always fail to quantify these details. In addition, these metrics evaluate fused images with the sources, they do not work if the number of source images is larger than the default (usually two). To deal with these problems, the last four metrics (i.e. *LIF*, *AG*, *MSD* and *GLD*) are used merely to measure the features of fused images in spite of the sources. And they are more reliable in terms of whether the boundaries are clear [2].

4.2.2. Quantitative Comparison

In this part, the average performance of MFIF-GAN on Lytro, MFFW and grayscale datasets will be compared with these representative SOTAs using the above evaluation metrics. The specific results is shown in Tab.1.

Based on the Lytro dataset, firstly, it can be clearly seen that on the first eight traditional metrics, our proposed MFIF-GAN trained on the α -matte dataset is generally superior to the other methods. Moreover, on the last four metrics which evaluate the quality around FDB, MFIF-GAN can still take the lead in addition to the MMF-Net which is specially designed and optimized for the DSE. The absolute advantage of our MFIF-GAN compared with the other SOTAs is obviously listed based on the MFFW. As for the grayscale dataset, our method can also stay ahead with the Quadtree generally.

4.2.3. Visual Comparison of Details

People pay more attention to the details on the premise that the overall fusion result is good. So the detailed contrast of these algorithms are provided visually on the 20th image in Lytro and the 11th in MFFW as shown in Fig.4. The superiority of MFIF-GAN is illustrated intuitively, especially in the region around the FDB.

Furthermore, by comparing the Fig.4(h) and 4(i), 4(q) and 4(r) respectively, it can be seen that if I_A , as the input of ConvCRFs in the FuseGAN, is replaced with I_B suffers from DSE, the edge of the foreground object will be much clearer.

(a) Lytro

| | CNN | MMF-net | MWGF | Quadtree | DSIFT | CSR | NSCT | FuseGAN | MFIF-GAN |
|-----------------------|----------------|-----------------|----------------|----------|-----------------|----------|----------|----------------|-----------------|
| <i>MI</i> | <u>1.07075</u> | 0.92506 | 1.01685 | 1.05303 | <u>1.08438</u> | 0.99020 | 0.90903 | 1.05501 | 1.09446 |
| <i>TE</i> | <u>0.37853</u> | 0.36443 | 0.37221 | 0.37658 | <u>0.37925</u> | 0.37288 | 0.36594 | 0.37610 | 0.38034 |
| <i>NCIE</i> | <u>0.83933</u> | 0.83067 | 0.83603 | 0.83806 | <u>0.84021</u> | 0.83400 | 0.82957 | 0.83896 | 0.84097 |
| <i>Q_G</i> | 0.70763 | 0.64492 | <u>0.71059</u> | 0.69854 | 0.70118 | 0.69508 | 0.68305 | <u>0.70814</u> | 0.71786 |
| <i>Q_M</i> | <u>1.91707</u> | 1.42079 | 1.73044 | 1.87318 | <u>2.03527</u> | 1.63746 | 1.40236 | 1.77586 | 2.07952 |
| <i>SF</i> | -0.03422 | -0.00845 | -0.03875 | -0.02546 | <u>-0.02442</u> | -0.03371 | -0.03258 | -0.03629 | <u>-0.02324</u> |
| <i>Q_Y</i> | <u>0.97583</u> | 0.94947 | 0.97004 | 0.973990 | <u>0.97615</u> | 0.95141 | 0.9533 | 0.97419 | 0.97696 |
| <i>Q_{CB}</i> | <u>0.79612</u> | 0.74312 | 0.77483 | 0.78761 | 0.79886 | 0.76064 | 0.74455 | 0.784 | <u>0.79764</u> |
| <i>LIF</i> | 0.38740 | 0.38670 | 0.387790 | 0.38714 | <u>0.38694</u> | 0.38737 | 0.38959 | 0.38823 | <u>0.38698</u> |
| <i>AG</i> | 2.99603 | 3.09201 | 2.97081 | 3.02048 | <u>3.02212</u> | 2.97995 | 3.00927 | 3.00098 | <u>3.0266</u> |
| <i>MSD</i> | 0.07007 | 0.07059 | 0.07000 | 0.070130 | <u>0.07017</u> | 0.07001 | 0.07003 | 0.06999 | <u>0.07019</u> |
| <i>GLD</i> | 14.75660 | 15.23405 | 14.62293 | 14.87703 | <u>14.88406</u> | 14.67629 | 14.82605 | 14.77889 | <u>14.90642</u> |

(b) MFFW

| | CNN | MWGF | Quadtree | DSIFT | CSR | NSCT | FuseGAN | MFIF-GAN |
|-----------------------|----------------|----------------|----------------|-----------------|-----------------|----------------|----------------|-----------------|
| <i>MI</i> | 0.99738 | 0.96529 | <u>1.02036</u> | 0.98671 | 0.8907 | 0.78236 | <u>1.01877</u> | 1.06806 |
| <i>TE</i> | 0.364 | 0.35761 | <u>0.36466</u> | 0.35911 | 0.3475 | 0.34291 | <u>0.36908</u> | 0.37169 |
| <i>NCIE</i> | 0.83288 | 0.83086 | <u>0.83451</u> | 0.83298 | 0.8271 | 0.82123 | <u>0.83531</u> | 0.83716 |
| <i>Q_G</i> | 0.56866 | <u>0.60566</u> | 0.49265 | 0.63777 | 0.53382 | 0.56998 | <u>0.62866</u> | 0.56345 |
| <i>Q_M</i> | 1.94031 | 1.8218 | <u>2.08961</u> | <u>2.03046</u> | 1.88064 | 1.14658 | 1.83548 | 2.21075 |
| <i>SF</i> | -0.05251 | -0.05472 | -0.04142 | <u>-0.03498</u> | <u>-0.03717</u> | -0.04652 | -0.04685 | -0.03111 |
| <i>Q_Y</i> | 0.96754 | <u>0.97207</u> | 0.96834 | 0.93459 | 0.86835 | 0.91066 | <u>0.97554</u> | 0.97939 |
| <i>Q_{CB}</i> | 0.74025 | 0.74085 | <u>0.75113</u> | 0.72927 | 0.69403 | 0.67343 | <u>0.74159</u> | 0.75624 |
| <i>LIF</i> | 0.38654 | 0.38852 | <u>0.38617</u> | 0.38884 | 0.38709 | 0.38626 | <u>0.38522</u> | 0.38361 |
| <i>AG</i> | 3.53508 | 3.51182 | 3.60422 | <u>3.62413</u> | 3.63075 | 3.59994 | 3.55498 | <u>3.62057</u> |
| <i>MSD</i> | 0.07931 | 0.07833 | 0.07857 | 0.07846 | 0.07843 | <u>0.07922</u> | 0.07879 | <u>0.07902</u> |
| <i>GLD</i> | 17.49452 | 17.36662 | 17.83513 | <u>17.92287</u> | 17.95869 | 17.80467 | 17.59685 | <u>17.91793</u> |

(c) grayscale

| | CNN | MWGF | Quadtree | DSIFT | CSR | NSCT | FuseGAN | MFIF-GAN |
|-----------------------|----------------|----------------|-----------------|-----------------|----------|-----------------|----------------|-----------------|
| <i>MI</i> | 1.1222 | 1.10868 | 1.15406 | <u>1.14503</u> | 1.04652 | 0.85708 | 1.07939 | <u>1.13731</u> |
| <i>TE</i> | 0.41359 | 0.41237 | <u>0.41746</u> | <u>0.41653</u> | 0.41127 | 0.38899 | 0.41031 | 0.41859 |
| <i>NCIE</i> | 0.8376 | 0.83731 | 0.83957 | <u>0.83889</u> | 0.83307 | 0.82378 | 0.83649 | <u>0.83899</u> |
| <i>Q_G</i> | 0.67711 | <u>0.67974</u> | 0.63484 | <u>0.68076</u> | 0.67628 | 0.63163 | 0.61953 | 0.68343 |
| <i>Q_M</i> | 2.33876 | 2.32259 | 2.46421 | <u>2.44523</u> | 2.22342 | 1.55645 | 1.73248 | <u>2.3914</u> |
| <i>SF</i> | -0.0414 | -0.04321 | <u>-0.03422</u> | -0.0353 | -0.03964 | -0.03928 | 0.02467 | <u>-0.03342</u> |
| <i>Q_Y</i> | <u>0.97724</u> | <u>0.97809</u> | 0.97873 | 0.97517 | 0.93837 | 0.93601 | 0.95378 | 0.97348 |
| <i>Q_{CB}</i> | <u>0.76327</u> | 0.76461 | 0.76313 | <u>0.76427</u> | 0.72702 | 0.7029 | 0.74415 | 0.7558 |
| <i>LIF</i> | 0.47571 | 0.47552 | <u>0.47551</u> | 0.47556 | 0.47578 | <u>0.47465</u> | 0.49394 | 0.47458 |
| <i>AG</i> | 3.53597 | 3.53821 | <u>3.56883</u> | <u>3.5687</u> | 3.52606 | 3.58797 | 3.54217 | <u>3.56084</u> |
| <i>MSD</i> | 0.13997 | 0.13984 | 0.14002 | 0.14009 | 0.13987 | <u>0.14014</u> | 0.15071 | <u>0.14064</u> |
| <i>GLD</i> | 17.15701 | 17.1702 | <u>17.31683</u> | <u>17.31368</u> | 17.10948 | 17.42544 | 17.1133 | <u>17.27329</u> |

Table 1: Averaged scores of fusion result based on Lytro, MFFW and grayscale datasets by various algorithms on 12 metrics. The best, the second, and the third best results are highlighted in bold, double underlining, and underlining, respectively.

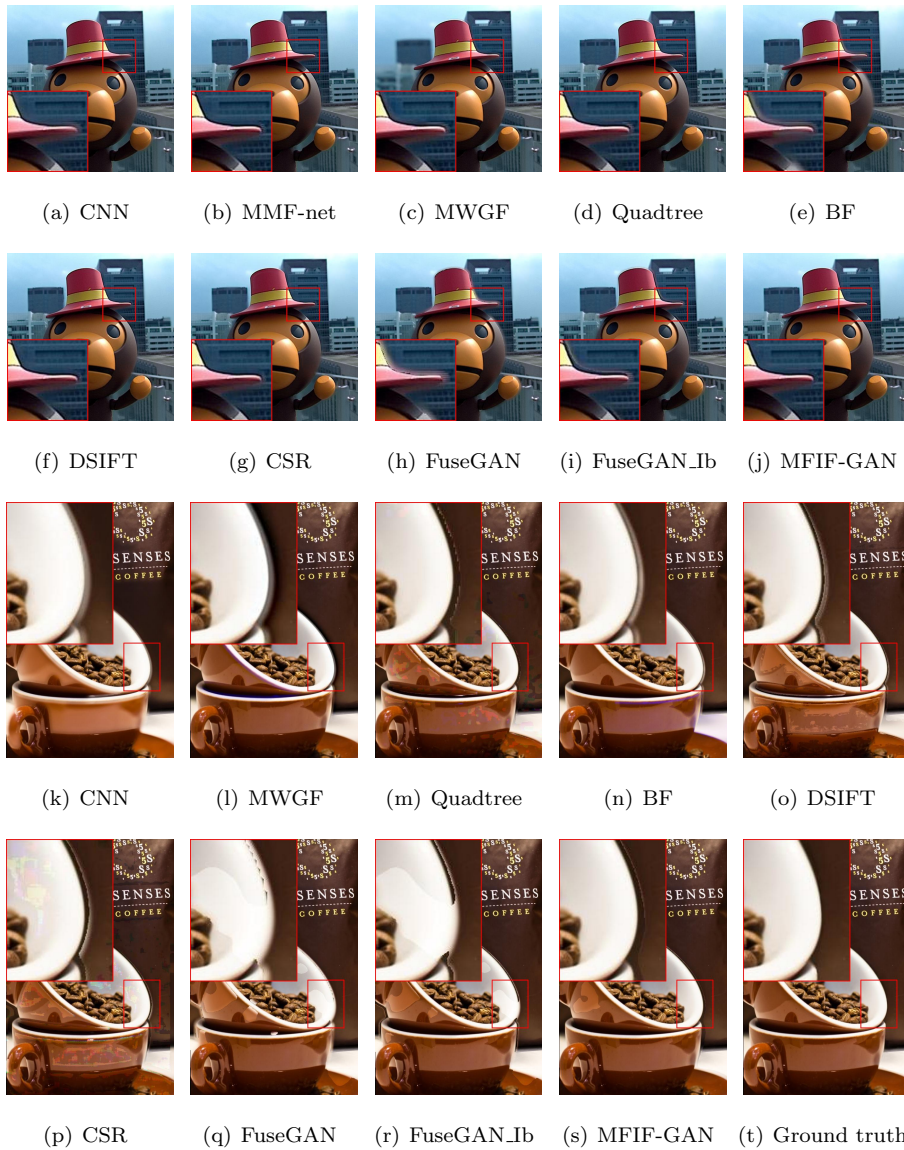


Figure 4: The fusion results on Lytro (20th) and MFFW (11th) with detail magnified of all algorithms. The FuseGAN_Ib exhibits the fusion result by FuseGAN with ConvCRF which feed with I_B as ground truth.

4.2.4. Solution to Mitigating the DSE

In this section, by comparing the details of the background and foreground about the baseline work FuseGAN and our MFIF-GAN, we illustrated the solution of our method to mitigating the DSE.

As we discussed above, when the all-in-focus image do not exist, the I_A has to be used as ground truth for the ConvCRFs in the FuseGAN. However, the DSE will vanish when it comes to I_A , which means the FDB in I_A is definitely clear. Thus the output of this algorithm is a focus map which has a sharp edge of real foreground objects. According to the α -matte model theory and the experience in daily observation, using this focus map will result in two completely different situations in the procedure of extracting clear information from the pair of source images:

When I_A is processed, the extracted foreground region is ideal. In contrast, when it comes to I_B , because of the existence of DSE, there will be a part of the foreground information diffuses into the background. So the diffusion laying outside the foreground objects will remain in the clear background (as shown clearly in the Fig.4(h) and 4(q)). So there will be a fuzzy FDB region, which is the diffusion of the foreground in I_B in essential. That partially explains why the undesirable result can be alleviated to some extend when I_A is substituted with I_B , as shown in Fig.4(i) and 4(r).

Actually, this part of the information about the clear background from the real edge to the diffuse edge is indeed missed as it is covered by the diffusion of the foreground in figure I_B . That is exactly the consequence of the DSE, which can not be eliminate absolutely. Moreover, this region is irregular, as its width is affected by the shape of the foreground and the distance from different positions to the sensor. So it is extremely complex and nontrivial to ideally handle the FDB region.

One of the solutions is to generate focus maps which are mildly larger than the real foreground objects. Using these focus maps can remain the background information around the foreground in I_A . Actually, the foreground region of

focus maps obtained by MFIF-GAN is a little larger than the corresponding foreground object, which is exactly what we expected.

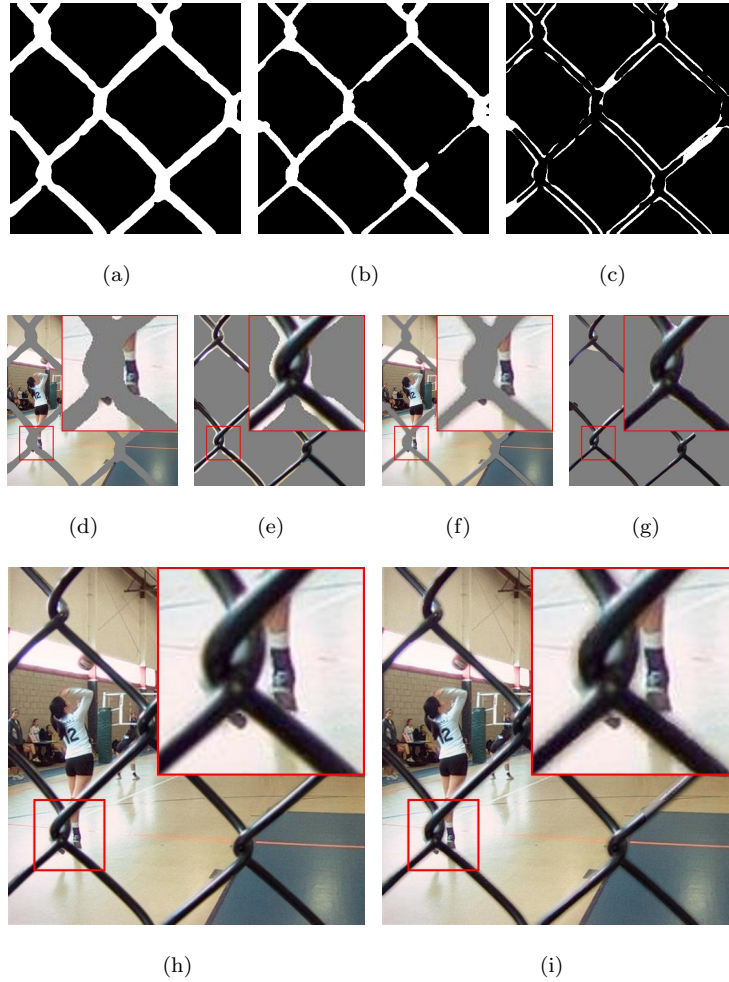


Figure 5: (a) exhibits the \hat{F}_{final} generated by MFIF-GAN with SRR; (b) shows the \hat{F}_{final} produced by FuseGAN with ConvCRF; (c) is the difference between two focus maps; (d) and (e) shows the background and foreground extracted respectively by \hat{F}_{final} in (a); (f) and (g) are the counterparts extracted by \hat{F}_{final} in (b); (h) and (i) are fusion results of MFIF-GAN and FuseGAN respectively with detail magnified.

Then, to illustrate this statement, we make the difference between two sets of focus maps which produced by baseline FuseGAN and MFIF-GAN respectively.

As shown in Fig.5(c), the appearance of white edges indicates this statement obviously. This characteristic brings MFIF-GAN with admirable performance around the FDB.

In order to show the improvement brought by this characteristic more clearly and intuitively, we used these two focus maps respectively to extract the foreground and background of the pair of source images. As shown in Fig.5(d) and 5(e), the background extracted by the larger focus map generated by MFIF-GAN eliminates partially the edge dispersion from the fuzzy foreground to the clear background, that is DSE. Meanwhile the extracted foreground contains part of the blurred background which can smooth the FDB. In contrast, as shown clearly in Fig.5(f) and 5(g), even though the foreground extracted by the focus map generated by FuseGAN seems to be ideal, the extracted background in Fig.5(f) retains DSE around the edge.

4.2.5. Execution Time

This section is about the comparison of computational efficiency. Instead of using complex computations, MFIF-GAN employs tensor operations that simply import model parameters trained previously, so the advantages of parallel computing can greatly increase the computational efficiency. Tab.2 lists the mean execution time of each method on the testing datasets. The experiments are carried out on a computer with Intel Core i7-10700K CPU @ 3.8GHz and RTX 2080ti GPU.

| | CNN | MWGF | Quadtrees | DSIFT | CSR | NSCT | FuseGAN | MFIF-GAN |
|-----------|---------|--------|-----------|--------|----------|--------|---------|---------------|
| Lytro | 25.6188 | 1.9677 | 0.5416 | 0.9095 | 120.9291 | 1.7989 | 0.4976 | 0.2229 |
| MFFW | 28.6874 | 2.2521 | 0.4922 | 1.6303 | 139.3664 | 2.2881 | 0.5019 | 0.2236 |
| grayscale | 18.0621 | 0.4808 | 0.3029 | 0.7909 | 28.9021 | 0.4929 | 0.2883 | 0.1344 |

Table 2: Averaged used time comparison of methods for pre-pair images fusion (unit: seconds)

Because the fusion results of MMF-net are used directly, this method is not involved in the comparison. FuseGAN needs extra post-processing, so we record the time with respect to the generation of the initial focus maps, post-

processing for refinement and final fusion. The average time used are (Lytro) 0.2135s, 0.2355s, 0.0486s; (MFFW2) 0.2156s, 0.2393s, 0.047s; (grayscale) 0.078s, 0.1969s, 0.0133s respectively.

4.3. Ablation Experiments

As mentioned above, the contributions of this paper includes a new network with attention module and gradient penalty as loss function, the simple but effective post-processing strategy and training the network on an α -matte dataset. To validate the effectiveness of these contributions, a series of ablation experiments are conducted here. Tab.3 list the results and discussions are reported below.

Firstly, the gradient penalty is removed in the loss function of the discriminator to show the effect brought by this regularization module. From the first column in Tab.3 we can see this part of loss function can also enhance the ability of the algorithm.

To evaluate the validity for the usage of post-processing SRR, this refinement procedure is removed in MFIF-GAN. The numerical results are shown in the second column in Tab.3. It can be intuitively observed that with this simple and effective processing, the performance of our model can be improved significantly.

Then, the SE-ResNet block is replaced by general ResNet to prove the improvement brought by attention mechanism. And the test result is listed in the third column in Tab.3. We can see that MFIF-GAN with SE-ResNet achieves better performance than the network without SE-block in residual module.

Finally, in order to verify the effectiveness of the α -matte model, we generate the conventional MFIF training dataset also based on VOC 2012 using the focus map directly. Our model is trained on both datasets. As shown in last two columns in Tab.3, MFIF-GAN performed better than the counterpart trained on the conventional MFIF dataset generally, which means the new α -matte dataset really promotes the performance of our method.

(a) Lytro

| | gp | pp | attention | alpha | MFIF-GAN |
|-------------|-----------------|-----------------|-----------------|-----------------|-----------------|
| <i>MI</i> | 1.09352 | 1.09168 | <u>1.09401</u> | <u>1.09433</u> | 1.09446 |
| <i>TE</i> | 0.3801 | 0.38005 | <u>0.38017</u> | <u>0.38021</u> | 0.38034 |
| <i>NCIE</i> | 0.84088 | 0.84078 | <u>0.8409</u> | <u>0.84092</u> | 0.84097 |
| <i>QG</i> | 0.70389 | 0.71942 | <u>0.71506</u> | 0.71307 | <u>0.71786</u> |
| <i>QM</i> | <u>2.08316</u> | 2.07665 | 2.08605 | <u>2.07986</u> | 2.07952 |
| <i>SF</i> | <u>-0.02378</u> | -0.02579 | <u>-0.02356</u> | -0.02396 | -0.02324 |
| <i>QY</i> | 0.97693 | 0.97633 | 0.97703 | <u>0.97697</u> | 0.97696 |
| <i>QCB</i> | 0.79719 | <u>0.79787</u> | <u>0.79803</u> | 0.79821 | 0.79764 |
| <i>LIF</i> | 0.387 | 0.38695 | <u>0.386977</u> | <u>0.386976</u> | 0.38698 |
| <i>AG</i> | 3.02369 | 3.02096 | <u>3.02427</u> | <u>3.02433</u> | 3.0266 |
| <i>MSD</i> | 0.07018 | <u>0.070192</u> | 0.07019 | <u>0.070191</u> | 0.07019 |
| <i>GLD</i> | 14.8918 | 14.87891 | <u>14.89462</u> | <u>14.89511</u> | 14.90642 |

(b) MFFW

| | gp | pp | attention | alpha | MFIF-GAN |
|-------------|----------------|-----------------|-----------------|-----------------|-----------------|
| <i>MI</i> | 1.05794 | 1.04143 | <u>1.05978</u> | <u>1.0643</u> | 1.06806 |
| <i>TE</i> | 0.36933 | 0.36768 | <u>0.37032</u> | <u>0.37025</u> | 0.37169 |
| <i>NCIE</i> | <u>0.83667</u> | 0.83524 | 0.83626 | <u>0.83668</u> | 0.83716 |
| <i>QG</i> | 0.62754 | 0.52553 | <u>0.60628</u> | <u>0.56972</u> | 0.56345 |
| <i>QM</i> | 2.1871 | 2.15102 | <u>2.20096</u> | <u>2.20705</u> | 2.21075 |
| <i>SF</i> | -0.03829 | <u>-0.03724</u> | -0.04244 | <u>-0.03358</u> | -0.03111 |
| <i>QY</i> | 0.97357 | 0.97256 | <u>0.9748</u> | <u>0.97766</u> | 0.97939 |
| <i>QCB</i> | 0.75139 | 0.74711 | <u>0.75394</u> | <u>0.75327</u> | 0.75624 |
| <i>LIF</i> | 0.38595 | <u>0.38393</u> | 0.38302 | 0.38404 | <u>0.38361</u> |
| <i>AG</i> | <u>3.61997</u> | 3.56963 | <u>3.60855</u> | 3.60173 | 3.62057 |
| <i>MSD</i> | 0.07852 | <u>0.0788</u> | 0.0785 | <u>0.07899</u> | 0.07902 |
| <i>GLD</i> | <u>17.9138</u> | 17.66934 | <u>17.85747</u> | 17.82522 | 17.91793 |

(c) grayscale

| | gp | pp | attention | alpha | MFIF-GAN |
|-------------|-----------------|-----------------|-----------------|----------------|-----------------|
| <i>MI</i> | <u>1.12951</u> | 1.12683 | <u>1.13147</u> | 1.12119 | 1.13731 |
| <i>TE</i> | <u>0.4176</u> | 0.41613 | 0.41757 | <u>0.41555</u> | 0.41859 |
| <i>NCIE</i> | <u>0.83859</u> | 0.83771 | <u>0.838</u> | 0.83772 | 0.83899 |
| <i>QG</i> | 0.68343 | <u>0.68267</u> | 0.68343 | <u>0.68274</u> | 0.68343 |
| <i>QM</i> | <u>2.38526</u> | 2.38042 | <u>2.38135</u> | 2.33375 | 2.3914 |
| <i>SF</i> | <u>-0.03346</u> | <u>-0.0337</u> | -0.03446 | -0.03839 | -0.03342 |
| <i>QY</i> | 0.97187 | <u>0.97251</u> | 0.97366 | 0.97118 | <u>0.97348</u> |
| <i>QCB</i> | 0.75094 | <u>0.75647</u> | 0.75936 | 0.75528 | <u>0.7558</u> |
| <i>LIF</i> | <u>0.47474</u> | 0.47486 | 0.47453 | 0.47505 | <u>0.47458</u> |
| <i>AG</i> | 3.55747 | <u>3.55946</u> | <u>3.55849</u> | 3.53625 | 3.56084 |
| <i>MSD</i> | 0.14061 | <u>0.14065</u> | 0.14066 | 0.14047 | <u>0.14064</u> |
| <i>GLD</i> | 17.25721 | <u>17.26601</u> | <u>17.25855</u> | 17.15341 | 17.27329 |

Table 3: Averaged scores of fusion results based on Lytro, MFFW and grayscale datasets in ablation experiments. The best, the second, and the third best results are highlighted in bold, double underlining, and underlining, respectively. The first two columns are MFIF-GAN without gradient penalty and post-processing. The attention in third column is the model in which the SE-ResNet block is replaced by ResNet And the alpha represents the MFIF-GAN trained by the conventional MFIF dataset without using the α -matte model.

4.4. Discussions of Experiments

From above of the ablation experiments, each of these factors contributes to the performance of the results to some extent, but generally none of them is more crucial than others.

By combining the Tab.1 and Tab.3, it is most worthy to note that without any one of factors, our algorithm still has a big advantage over other SOTAs, which indicates that proposed MFIF-GAN with a new architecture and reconstruction loss function has strong robustness for gradient regularization, attention mechanism and training dataset. It also shows that our work is able to get rid of over-dependence on the post-processing to some extent.

What is more, by comparing the results of the FuseGAN and MFIF-GAN which trained on the same conventional dataset, the FuseGAN as a baseline is still inferior to the MFIF-GAN generally.

5. Conclusions

In this paper, we propose a generative adversarial network termed MFIF-GAN for the MFIF task. The innovation is that attention mechanism is exploited in the network which has a new architecture with six branches to extract features. And the ℓ_1 -norm reconstruction loss and gradient penalty is creatively added to the optimization function to improve the quality of the outputs. Moreover, the SRR algorithm for post-processing is used to refine the initial focus maps in a computational effective way. Last but not least, based on a synthetic α -matte training dataset, this novel end-to-end color multi-focus image fusion algorithm can fuse more realistic images especially around the FDB. The essential point of our work is that the proposed method can guarantee the contents in generated focus maps are mildly larger than the corresponding foreground objects, which can simulate the DSE and further exactly avoid this annoying effect.

As a new fusion algorithm, the extensive experiments demonstrate that our MFIF-GAN is superior to other representative SOTA methods on visual per-

ception, quantitative analysis and efficiency, which can bring more satisfactory pretreatment to other computer vision tasks.

Acknowledgements

The research is supported by the National Key Research and Development Program of China under grant 2018AAA0102201, the National Natural Science Foundation of China under grant 61877049, 61976174 and 11671317.

References

- [1] N. Salvaggio, Basic Photographic Materials and Processes, Taylor & Francis, 2009.
- [2] S. Xu, X. Wei, C. Zhang, J. Liu, J. Zhang, Mffw: A new dataset for multi-focus image fusion, arXiv preprint arXiv:2002.04780.
- [3] A. A. Goshtasby, S. Nikolov, Image fusion: advances in the state of the art, *Information fusion* 2 (8) (2007) 114–118.
- [4] I. De, B. Chanda, B. Chattopadhyay, Enhancing effective depth-of-field by image fusion using mathematical morphology, *Image and Vision Computing* 24 (12) (2006) 1278–1287.
- [5] T. Stathaki, *Image Fusion: Algorithms and Applications*, Elsevier, 2011.
- [6] Q. Zhang, B.-l. Guo, Multifocus image fusion using the nonsubsampling contourlet transform, *Signal processing* 89 (7) (2009) 1334–1346.
- [7] A. L. da Cunha, J. Zhou, M. N. Do, The nonsubsampling contourlet transform: Theory, design, and applications, *IEEE Trans. Image Processing* 15 (10) (2006) 3089–3101.
- [8] B. Yang, S. Li, Multifocus image fusion and restoration with sparse representation, *IEEE Transactions on Instrumentation and Measurement* 59 (4) (2009) 884–892.

- [9] Q. Zhang, M. D. Levine, Robust multi-focus image fusion using multi-task sparse representation and spatial context, *IEEE Transactions on Image Processing* 25 (5) (2016) 2045–2058.
- [10] Y. Liu, S. Liu, Z. Wang, A general framework for image fusion based on multi-scale transform and sparse representation, *Information Fusion* 24 (2015) 147–164.
- [11] H. Ma, Q. Liao, J. Zhang, S. Liu, J. Xie, An α -matte boundary defocus model based cascaded network for multi-focus image fusion, *CoRR* abs/1910.13136. [arXiv:1910.13136](https://arxiv.org/abs/1910.13136).
- [12] I. De, B. Chanda, Multi-focus image fusion using a morphology-based focus measure in a quad-tree structure, *Information Fusion* 14 (2) (2013) 136–146.
- [13] X. Guo, R. Nie, J. Cao, D. Zhou, L. Mei, K. He, Fusegan: Learning to fuse multi-focus image via conditional generative adversarial network, *IEEE Trans. Multimedia* 21 (8) (2019) 1982–1996.
- [14] K. He, J. Sun, X. Tang, Guided image filtering, in: *European Conference on Computer Vision*, Springer, 2010, pp. 1–14.
- [15] X. Bai, Y. Zhang, F. Zhou, B. Xue, Quadtree-based multi-focus image fusion using a weighted focus-measure, *Information Fusion* 22 (2015) 105–118.
- [16] Y. Zhang, X. Bai, T. Wang, Boundary finding based multi-focus image fusion through multi-scale morphological focus-measure, *Information Fusion* 35 (2017) 81–101.
- [17] Y. Liu, X. Chen, H. Peng, Z. Wang, Multi-focus image fusion with a deep convolutional neural network, *Information Fusion* 36 (2017) 191–207.
- [18] R. Guo, X.-j. Shen, X.-y. Dong, X.-l. Zhang, Multi-focus image fusion based on fully convolutional networks, *Frontiers of Information Technology & Electronic Engineering* 21 (7) (2020) 1019–1033.

- [19] H. Ma, J. Zhang, S. Liu, Q. Liao, Boundary aware multi-focus image fusion using deep neural network, in: 2019 IEEE International Conference on Multimedia and Expo (ICME), IEEE, 2019, pp. 1150–1155.
- [20] C. Du, S. Gao, Image segmentation-based multi-focus image fusion through multi-scale convolutional neural network, *IEEE Access* 5 (2017) 15750–15761.
- [21] J. Hu, L. Shen, G. Sun, Squeeze-and-excitation networks, in: Proceedings of the IEEE Conference on Computer Vision and Pattern Recognition (CVPR), 2018, pp. 7132–7141.
- [22] M. Everingham, S. A. Eslami, L. Van Gool, C. K. Williams, J. Winn, A. Zisserman, The pascal visual object classes challenge: A retrospective, *International Journal of Computer Vision* 111 (1) (2015) 98–136.
- [23] Y. Liu, X. Chen, Z. Wang, Z. J. Wang, R. K. Ward, X. Wang, Deep learning for pixel-level image fusion: Recent advances and future prospects, *Information Fusion* 42 (2018) 158–173.
- [24] W. Zhao, D. Wang, H. Lu, Multi-focus image fusion with a natural enhancement via a joint multi-level deeply supervised convolutional neural network, *IEEE Transactions on Circuits and Systems for Video Technology* 29 (4) (2018) 1102–1115.
- [25] B. Ma, X. Ban, H. Huang, Y. Zhu, Sef-fuse: An unsupervised deep model for multi-focus image fusion, CoRR abs/1908.01703. [arXiv:1908.01703](https://arxiv.org/abs/1908.01703).
- [26] F. A. Guerrero-Peña, P. D. Marrero-Fernández, T. I. Ren, G. C. Vasconcelos, A. Cunha, A multiple source hourglass deep network for multi-focus image fusion, CoRR abs/1908.10945. [arXiv:1908.10945](https://arxiv.org/abs/1908.10945).
- [27] M. Mirza, S. Osindero, Conditional generative adversarial nets, arXiv preprint [arXiv:1411.1784](https://arxiv.org/abs/1411.1784).

- [28] X. Mao, Q. Li, H. Xie, R. Y. Lau, Z. Wang, S. Paul Smolley, Least squares generative adversarial networks, in: Proceedings of the IEEE International Conference on Computer Vision, 2017, pp. 2794–2802.
- [29] Z. Huang, W. Xu, K. Yu, Bidirectional lstm-crf models for sequence tagging, arXiv preprint arXiv:1508.01991.
- [30] Y. Liu, S. Liu, Z. Wang, Multi-focus image fusion with dense SIFT, Information Fusion 23 (2015) 139–155.
- [31] A. Ghosh, H. Kumar, P. Sastry, Robust loss functions under label noise for deep neural networks, arXiv preprint arXiv:1712.09482.
- [32] K. He, X. Zhang, S. Ren, J. Sun, Deep residual learning for image recognition, in: Proceedings of the IEEE conference on computer vision and pattern recognition, 2016, pp. 770–778.
- [33] C. Szegedy, W. Liu, Y. Jia, P. Sermanet, S. Reed, D. Anguelov, D. Erhan, V. Vanhoucke, A. Rabinovich, Going deeper with convolutions, in: Proceedings of the IEEE conference on computer vision and pattern recognition, 2015, pp. 1–9.
- [34] H. Zhang, Z. Le, Z. Shao, H. Xu, J. Ma, Mff-gan: An unsupervised generative adversarial network with adaptive and gradient joint constraints for multi-focus image fusion, Information Fusion 66 (2020) 40–53.
- [35] I. Goodfellow, J. Pouget-Abadie, M. Mirza, B. Xu, D. Warde-Farley, S. Ozair, A. Courville, Y. Bengio, Generative adversarial nets, in: Advances in neural information processing systems, 2014, pp. 2672–2680.
- [36] S. Ioffe, C. Szegedy, Batch normalization: Accelerating deep network training by reducing internal covariate shift, arXiv preprint arXiv:1502.03167.
- [37] M. Arjovsky, S. Chintala, L. Bottou, Wasserstein gan, arXiv preprint arXiv:1701.07875.

- [38] I. Gulrajani, F. Ahmed, M. Arjovsky, V. Dumoulin, A. C. Courville, Improved training of wasserstein gans, in: *Advances in neural information processing systems*, 2017, pp. 5767–5777.
- [39] M. Nejati, S. Samavi, S. Shirani, Multi-focus image fusion using dictionary-based sparse representation, *Information Fusion* 25 (2015) 72–84.
- [40] Y. Liu, L. Wang, J. Cheng, C. Li, X. Chen, Multi-focus image fusion: A survey of the state of the art, *Information Fusion* 64 (2020) 71–91.
- [41] Y. Liu, X. Chen, R. K. Ward, Z. J. Wang, Image fusion with convolutional sparse representation, *IEEE Signal Process. Lett.* 23 (12) (2016) 1882–1886.
- [42] Z. Zhou, S. Li, B. Wang, Multi-scale weighted gradient-based fusion for multi-focus images, *Information Fusion* 20 (2014) 60–72.
- [43] Guihong Qu, Dali Zhang, Pingfan Yan, Information measure for performance of image fusion, *Electronics Letters* 38 (7) (2002) 313–315.
- [44] N. Cvejic, C. N. Canagarajah, D. R. Bull, Image fusion metric based on mutual information and tsallis entropy, *Electronics Letters* 42 (11) (2006) 626–627.
- [45] T. Stathaki, *Image fusion: algorithms and applications*, Elsevier, 2011.
- [46] C. Xydeas, , V. Petrovic, Objective image fusion performance measure, *Electronics letters* 36 (4) (2000) 308–309.
- [47] P.-w. Wang, B. Liu, A novel image fusion metric based on multi-scale analysis, in: *2008 9th International Conference on Signal Processing*, IEEE, 2008, pp. 965–968.
- [48] Y. Zheng, E. A. Essock, B. C. Hansen, A. M. Haun, A new metric based on extended spatial frequency and its application to DWT based fusion algorithms, *Information Fusion* 8 (2) (2007) 177–192.

- [49] C. Yang, J. Zhang, X. Wang, X. Liu, A novel similarity based quality metric for image fusion, *Information Fusion* 9 (2) (2008) 156–160.
- [50] Y. Chen, R. S. Blum, A new automated quality assessment algorithm for image fusion, *Image Vision Comput.* 27 (10) (2009) 1421–1432.
- [51] X. Bai, F. Zhou, B. Xue, Noise-suppressed image enhancement using multiscale top-hat selection transform through region extraction, *Appl. Opt.* 51 (3) (2012) 338–347.
- [52] G. Cui, H. Feng, Z. Xu, Q. Li, Y. Chen, Detail preserved fusion of visible and infrared images using regional saliency extraction and multi-scale image decomposition, *Optics Communications* 341 (2015) 199 – 209.
- [53] Z. Liu, E. Blasch, Z. Xue, J. Zhao, R. Laganière, W. Wu, Objective assessment of multiresolution image fusion algorithms for context enhancement in night vision: A comparative study, *IEEE Trans. Pattern Anal. Mach. Intell.* 34 (1) (2012) 94–109.